

Probing the coherence of solid-state qubits at avoided crossings

Mykyta Onizhuk,^{1,2} Kevin C. Miao,² Joseph P. Blanton,^{3,2} He Ma,^{1,2} Christopher P. Anderson,² Alexandre Bourassa,² David D. Awschalom,^{3,2,4} and Giulia Galli^{1,2,4,*}

¹*Department of Chemistry, University of Chicago, Chicago, IL 60637, USA*

²*Pritzker School of Molecular Engineering,
University of Chicago, Chicago, IL 60637, US*

³*Department of Physics, University of Chicago, Chicago, IL 60637, USA*

⁴*Materials Science Division and Center for Molecular Engineering,
Argonne National Laboratory, Lemont, IL 60439, USA*

(Dated: August 16, 2021)

Abstract

Optically addressable paramagnetic defects in wide-band-gap semiconductors are promising platforms for quantum communications and sensing. The presence of avoided crossings between the electronic levels of these defects can substantially alter their quantum dynamics and be both detrimental and beneficial for quantum information applications. Avoided crossings give rise to clock transitions, which can significantly improve protection from magnetic noise and favorably increase coherence time. However, the reduced coupling between electronic and nuclear spins at an avoided crossing may be detrimental to applications where nuclear spins act as quantum memories.

Here we present a combined theoretical and experimental study of the quantum dynamics of paramagnetic defects interacting with a nuclear spin bath at avoided crossings. We develop a computational approach based on a generalization of the cluster expansion technique, which can account for processes beyond pure dephasing and describe the dynamics of any solid-state spin-qubits near avoided crossings. Using this approach and experimental validation, we determine the change in nature and source of noise at avoided crossings for divacancies in SiC. We find that we can condition the clock transition of the divacancies in SiC on multiple adjacent nuclear spins states. In our experiments, we demonstrate that one can suppress the effects of fluctuating charge impurities with depletion techniques, leading to an increased coherence time at clock transition, limited purely by magnetic noise. Combined with *ab-initio* predictions of spin Hamiltonian parameters, the proposed theoretical approach paves the way to designing the coherence properties of spin qubits from first principles.

I. INTRODUCTION

In search of solid-state qubits, electron spin defects in wide-band-gap semiconductors have been extensively explored as robust quantum systems offering both long coherence times [1] and optical read-out [2] capabilities for quantum information [3] and quantum sensing [4] applications. In order to design optimal qubits, it is critical to understand and control the interaction between the central electronic spin and the nuclear spin bath. The latter determines, at least in part, the coherence time of qubits, as observed in many solid-

* Corresponding author gagalli@uchicago.edu

state color centers [5–8], but it also offers a platform for robust multiqubit registers for the development of quantum networks [9–12].

The description of the interaction between a central spin and the nuclear bath can be particularly challenging when avoided crossings between energy levels of the central spin occur. Avoided crossings give rise to regimes that can be both beneficial and deleterious to the qubit’s coherence. For example, operating at the minimum of the spin transition frequency can significantly increase the coherence time when clock transitions arise [13–15]. On the other hand, spin ground state level anticrossings may lead to an undesired increase in longitudinal relaxation rates [16, 17] of spin defects. A unified formalism to simulate on equal footing the dynamics of qubits under different conditions is not readily available.

Here we present a theoretical approach to predict the adiabatic dynamics of a qubit interacting with nuclear baths at clock transitions and near ground state level anti-crossings (GSLAC) and validate our predictions experimentally. In particular, we suggest ways to design and optimize the electron-nuclear spin interactions in clock-transition-based quantum devices. Our approach, based on the generalization of the cluster-correlation expansion method [18], is general and applicable to a broad class of spin defects.

We focus on neutral divacancies ($V_C V_{Si}$) in silicon carbide (SiC), which are promising spin qubit candidates [19–22]. In particular, the axial divacancy is one of the most commonly studied defect qubits in SiC [23, 24], with purely axial zero field splitting. The basal divacancy, on the other hand, exhibits both an axial and transverse crystal field splitting component, giving rise to clock transitions at zero magnetic field [15, 25]. We validate our predictions by carrying out Ramsey and Hahn-echo experiments on the basal divacancy, as well as by comparing our theoretical results to previous measurements [5]. Using theory and experiment we show that in the presence of strongly coupled nuclear spins, multiple clock transition conditioned on the nuclear spin state may occur. Importantly, we identify the dominant causes of decoherence at avoided crossings and clock transitions, and we discuss the nature of the noise as a function of the magnetic field. Finally, we show experimentally that the impact of the nuclear bath on the qubit dynamics can be isolated by employing a charge depletion technique, which leads to an increase of spin coherence time of clock transition qubits by suppressing electric noise.

The rest of the paper is organized as follows: in Sec. II we summarize the proposed theoretical approach. Next, we discuss the decoherence of axial divacancy near GSLAC in

Sec. III. Sec. IV contains the Ramsey and Hahn-echo predictions and measurements for basal divacancy near clock transition. We describe a change in nature of the noise near avoided crossings in Sec. V, and in Sec. VI we discuss further ways to engineer coherence protections. Finally, we conclude the paper in Sec. VII discussing the general implications of our findings.

II. THEORETICAL FRAMEWORK

We start by describing a generalization of the cluster-correlation expansion (CCE) method, and we then apply it to specific defects in SiC.

The CCE method is one of the leading approaches for the simulation of quantum dynamics of spin-qubits interacting with a multitude of bath spins [5, 26–28]. The method approximates the off-diagonal elements of the qubit density matrix as a product of contributions from independent nuclear spin clusters (Fig.1a). In its conventional formulation, the CCE method is not appropriate to describe clock transitions [29], as it does not account for long-range interactions between the bath spins mediated by the central electron spin [30]; in addition, it cannot describe transitions between spin levels that are close in energy, where the nuclear bath can induce flips of the central spin [31]. A generalization of the CCE approach was recently proposed to address the longitudinal relaxation of the NV^- center in diamond [18]. In this formulation, each nuclear cluster includes the central spin explicitly, and the cluster contributions are used to compute the change in population of the qubit states. In this work, we both reformulate the generalized CCE method and include a Monte-Carlo bath state sampling (gCCE, Fig.1b), thus enabling the prediction of the dynamics of both the population and the coherence of the central spin at avoided crossings.

A. Spin defect Hamiltonian

The Hamiltonian of a central electron spin interacting with a bath of nuclear spins in an external magnetic field can be written as a sum of the central spin Hamiltonian \hat{H}_e , and nuclear Zeeman splitting, hyperfine coupling, and nuclear dipolar coupling terms:

$$\hat{H} = \hat{H}_e - \sum_i \gamma_{n,i} B_z \hat{I}_{z,i} + \sum_i \mathbf{S} \mathbf{A} \mathbf{I}_i + \sum_{i \neq j} \mathbf{I}_i \mathbf{P} \mathbf{I}_j \quad (1)$$

Here B_z is the magnetic field oriented along the z axis, $\gamma_{n,i}$ is the gyromagnetic ratio of the i -th nuclear spin, $\mathbf{S} = (\hat{S}_x, \hat{S}_y, \hat{S}_z)$ and $\mathbf{I}_i = (\hat{I}_{x,i}, \hat{I}_{y,i}, \hat{I}_{z,i})$ denote electron and the i -th nuclear spin operators respectively, \mathbf{A}_i is the hyperfine coupling tensor of the i -th nuclear spin, and \mathbf{P}_{ij} is the dipole-dipole coupling between spins i and j .

The electron Hamiltonian \hat{H}_e includes the Zeeman interaction with the external magnetic field and a zero field splitting (ZFS) term with longitudinal (D) and transverse (E) components:

$$\hat{H}_e = -\gamma_e B_z \hat{S}_z + D \left(\hat{S}_z^2 - \frac{1}{3} S(S+1) \right) + E(\hat{S}_x^2 - \hat{S}_y^2) \quad (2)$$

B. Generalization of cluster-correlation expansion method

In the gCCE method, we compute both diagonal and off-diagonal elements of the density matrix of the central spin $\rho_{ab} = \langle a | \hat{\rho} | b \rangle$ as the product of cluster contributions, where a, b denote different spin states (e.g. $m_s = 1, 0, -1$ states for spin 1 systems):

$$\rho_{ab} = \tilde{\rho}_{ab}^{\{0\}} \prod_i \tilde{\rho}_{ab}^{\{i\}} \prod_{i,j} \tilde{\rho}_{ab}^{\{ij\}} \dots \quad (3)$$

Here $\{0\}$ denotes a cluster consisting of a free central spin, $\{i\}$ a cluster including the central spin and nuclear spin i , and so on. The maximum size of the cluster in Eq. (3) defines the order of the approximation. For example, at first order (gCCE1), only isolated nuclear spins ($\rho^{\{i\}}$) are included in the expansion. At second order (gCCE2), contributions from pairs of nuclear spins ($\rho^{\{i,j\}}$) are added, etc. The cluster contributions are defined recursively:

$$\tilde{\rho}_{ab}^{\{C\}} = \frac{\langle a | \hat{\rho}_C(t) | b \rangle}{\prod_{C'} \tilde{\rho}_{ab}^{\{C' \subset C\}}} \quad (4)$$

Where $\rho_C(t)$ is the density matrix of the cluster C , the superscript $\{C'\}$ indicates all sub-clusters of C , including the free central spin sub-cluster $\{0\}$. The density matrix $\rho_C(t)$ is computed using the time ordered propagator:

$$\hat{U}_C(t) = \mathcal{T} \left[e^{-i \int_0^t \hat{H}(\tau) d\tau} \right] \quad (5)$$

where the \mathcal{T} is the time ordering operator, and $\hat{H}(\tau)$ is the time dependent Hamiltonian, which includes only the interactions within a given cluster.

We emphasize that in our formulation we take into account the interaction of spins inside a given cluster with the rest of the bath, thus allowing for different energy splittings within a cluster, and improving the numerical convergence of cluster dynamic simulations [32]. In particular, we perform calculations with randomly sampled *pure* states of the spin bath, and for each pure state we include the mean-field effect of all the nuclear spins outside a chosen cluster \hat{H}_{mf} (Fig.1b). As we show below, the use of the Monte Carlo sampling of bath states is critical to explaining the dynamics of the central spin at avoided crossings. Further details are available in Appendix B.

III. DECOHERENCE AT GROUND STATE LEVEL ANTICROSSINGS

We start by investigating avoided crossings, and in particular we study the dynamics of the axial $kk\text{-}V_{\text{C}}V_{\text{Si}}$ defect in 4H-SiC near its GSLAC. The measured ensemble-averaged Hahn-echo coherence times (T_2) of this defect reaches 1.3 ms in samples with natural isotopic concentration [5]. Due to its C_{3v} symmetry, the ZFS entering (2) has only a longitudinal component $D = 1.305$ GHz [33], and the qubit levels may be chosen as the $|{-1}_z\rangle$ and $|0_z\rangle$ eigenstates of S_z , where z is the spin quantization axis.

The coherence time of the $kk\text{-}V_{\text{C}}V_{\text{Si}}$ divacancy was successfully predicted with the conventional CCE for a wide range of magnetic fields, and the homo-nuclear pair-wise spin flips were found to be the main source of decoherence at strong fields [5]. However, a significant decrease in the coherence time was observed in experiments when the magnetic field approaches ~ 45 mT; such a decrease is not captured by conventional CCE calculations (Fig.2b), suggesting a decoherence mechanism beyond pure dephasing.

We performed gCCE calculations with Monte Carlo sampling of bath states (Fig.2d) and we correctly obtained a local minimum in $T_2(B)$ for $B_z = 46.6$ mT, while reproducing the results of conventional CCE calculations for other values of B_z . We note that while previous CCE results [5] were obtained using a point dipole approximation, here we used accurate hyperfine couplings predicted by *ab initio* calculations (see Methods). This difference in hyperfine couplings accounts for the small discrepancy between CCE and gCCE results observed at small fields.

The origin of the minimum in $T_2(B)$ can be understood by analyzing the populations of different spin levels (Fig.2c). For most values of B , the population of the electron spin

levels is constant. However, there are values of B for which the energy difference between the $|1\rangle$ and $|0\rangle$ levels is of the same order of magnitude as the hyperfine interaction with nuclear spins. We note that when the energy splitting falls below ~ 100 MHz, significant deviations from pure dephasing starts to occur (see Supplementary Information). In this case, the electron spin experiences large population fluctuations which lead to a significant decrease in coherence time near the GSLAC. Therefore, we conclude that at a GSLAC, the longitudinal relaxation process substantially contributes to decreasing the Hahn-echo coherence time, as observed experimentally.

IV. DECOHERENCE AT CLOCK TRANSITIONS

As mentioned earlier, the basal divacancy $kh\text{-}V_C V_{Si}$ exhibits a clock transition at zero magnetic field. Compared to the Bi:Si donor qubits, studied in Ref.[29, 34], the clock transition in this defect arises from ZFS interactions. $kh\text{-}V_C V_{Si}$ has C_{1h} symmetry, leading to a nonzero transverse component of the ZFS: $E = 18.4$ MHz [25]. Combined with a strong longitudinal splitting ($D = 1.334$ GHz), the ZFS tensor leads to an avoided crossing of electron spin levels at zero magnetic field from which a clock transition emerges. The frequency of clock transitions is insensitive to magnetic fields to first order, thus increasing protection from the nuclear bath induced decoherence [14], but at the same time it may exhibit an increased sensitivity towards electric noise [35].

We applied the gCCE method with and without Monte Carlo bath state sampling to reveal the qubit dynamics observed in the Ramsey and Hahn-echo experiments. Figure 3 shows the time evolution of the off-diagonal element of the density matrix of the qubit for one random spatial configuration of nuclear spins. The qubit levels were chosen as the electron Hamiltonian eigenstates $|+\rangle = \frac{1}{\sqrt{2}}(|1_z\rangle + |-1_z\rangle)$ and $|0\rangle = |0_z\rangle$ at zero magnetic field, and the qubit was initially prepared in the $|\psi\rangle = \frac{1}{\sqrt{2}}(|+\rangle + |0\rangle)$ state. For $B \neq 0$, the eigenstate $|+\rangle$ evolves into a different superposition of $|1_z\rangle$ and $|-1_z\rangle$ (see Supplementary Information).

We emphasize that considering mean-field effects of nuclear interactions is crucial in order to obtain the correct dynamics of the coherent state. We found that the decay of the observed central spin Ramsey envelope can be accurately described by performing calculations at the gCCE1 level with Monte Carlo bath state sampling (Fig.3b). Since gCCE1

simulations do not explicitly include nuclear-nuclear interactions, our results suggest that in the Ramsey experiment the dominant decoherence mechanism is the static Overhauser field generated by nuclear spins, in agreement with Ref. [30]. On the other hand, we found that for most configurations, gCCE2 is necessary and sufficient to converge the value of the Hahn-echo coherence (Fig.3c) time, confirming the significant contribution of nuclear-nuclear interactions.

A. Impact of nuclear spin coupling

In order to understand how the coupling strength between the central spin and the nuclear spins affects clock transitions, we experimentally investigated three different single kh - $V_C V_{Si}$ divacancy qubits. They are labeled VVA, VVB, and VVC, and they represent configurations with weakly (VVA) and strongly interacting (VVB and VVC) nuclear spins. We obtained theoretical configurations directly comparable with the experimental ones by generating a set of random nuclear spin configurations in the SiC lattice with the same number of strongly interacting nuclear spins as observed in the measured Ramsey fringes. Out of this set we then selected the configurations with a computed value of T_2^* at $B_z = 50 \mu\text{T}$ similar to the measured one (see SI for details).

We first analyze the VVA configuration, which contains only weakly coupled nuclear spins. Its frequency spectrum, obtained as a Fourier transform of Ramsey fringe oscillations, can be simply represented by one hyperbola (Fig.4a, b). In the absence of a nuclear bath, the frequency of the clock transition is given by:

$$\omega - \omega_0 = \sqrt{\gamma_e^2 B_z^2 + E^2} \quad (6)$$

We obtain good agreement between theoretical predictions and the measured Ramsey fringes at small fields, but in the zero field regime the experimentally observed decoherence is significantly faster (Fig.4h). We found that this apparent discrepancy is due to the electric noise affecting the qubit state, as we explain below.

When operated near a clock transition, the basal divacancy spin becomes first-order insensitive to magnetic fluctuations. However, a first-order sensitivity to electric field fluctuations emerges, due to the linear dependence of the ZFS tensor components on the local electric field. Therefore, the electron spin dephasing time becomes limited by the electric field noise

[12, 15, 35]. In SiC divacancies the electric noise is primarily caused by charge state fluctuations of photoactive impurities, which may undergo charge state transitions under optical excitation [36, 37], leading to a variation of local electric fields.

In our experiments, we used charge depletion [25, 36] to deactivate photoactive impurities within the optical excitation region, thus substantially reducing the electric field contributions to the ground-state spin dephasing. We applied 13 V across a lithographically patterned capacitor with a 10 μm gap width. The applied electric field acting on a divacancy located between the capacitor plates ionizes the undesired charge carriers and removes them from photoactive impurities in the proximity of the divacancy. This technique allowed us to isolate the contributions of the magnetic field noise near the clock transition (Fig.4g) and to perform a meaningful comparison with our theoretical model.

We found that under charge depleted conditions, the measured coherence time is substantially increased and the experimentally observed Ramsey precession at zero field agrees well with the theoretical prediction of the gCCE. Interestingly, in the presence of a weak magnetic field, an agreement between theory and experiment is obtained without applying any charge depletion, indicating that the decoherence rate in this case is not limited by electric noise.

We now turn to lattice configurations with strongly coupled nuclear spins. We first consider the defect labeled VVB, for which we observe a splitting in the frequency spectrum due to the presence of one strongly coupled nuclear spin (Fig.4c, d). Each of the hyperbolae shown in the figure corresponds to the oscillation frequency of Ramsey fringes of the divacancy, coupled to either the spin-up or spin-down nuclear state. The minimum of each hyperbola occurs when the magnetic field is equal to the hyperfine field of the strongly coupled nuclear spin, $\left| \frac{A_{iz}}{2\gamma_e} \right| = |B_z|$ where $A_{iz} = \sqrt{A_{xz}^2 + A_{yz}^2 + A_{zz}^2}$ [25]. By solving this equation, we obtain the hyperfine parameter of the strongly coupled nuclear spin in VVB: $A_{iz} \approx 0.6$ MHz.

In Fig.4c, d we compare with experiments our theoretical results for a nuclear configuration for which the computed A_{iz} is 0.75 MHz. We find an excellent agreement for the time evolution and the frequency spectrum. We note that due to the presence of the strongly coupled spin, the Ramsey precession exhibits a fast and a slow decay mode (Fig.4i), and the full dynamics of the decoherence process may not be described by a single T_2^* (Fig.4j). However, by initializing the strongly coupled nuclear spin so that it is antiparallel to the ex-

ternal magnetic field, one can eliminate the fast decay mode, and, together with the charge depletion strategy outlined above, one may achieve a substantial increase (by a factor of 5) in the coherence time (see SI).

In the presence of several strongly coupled nuclear spins, further splitting of the frequency spectrum may occur. In this case, the minimum of each hyperbola is located at:

$$B_z = \sum_{\text{strong}} \pm \frac{A_{iz}}{2\gamma_e} \quad (7)$$

The measured frequency spectrum of the defect labeled VVC contains six separate hyperbolae, suggesting the presence of three strongly coupled nuclear spins with two of them having similar hyperfine parameters (Fig.4e, f). We identify one nuclear spin with $A_{iz} \approx 1.7$ MHz and two nuclear spins with $A_{iz} \approx 0.6$ MHz.

Hence, we compare theory and experiment using calculations for a nuclear configuration which contains 3 strongly coupled nuclear spins with similar values of the hyperfine constants: $A_{iz} = 1.92, 0.65, 0.49$ MHz. We obtain a good agreement in both the time and frequency domains. However, due to the complexity of the dynamics, a simple exponential decay cannot reliably characterize the decoherence time of VVC; nevertheless the decoherence occurs on a timescale of 200-300 μs , both in theory and experiment.

Furthermore, we carried out a study of the Hahn-echo decoherence time for the VVA and VVB defects (Fig.5a, b) and again found excellent agreement between experimental values and theoretical predictions. In VVB, the presence of the strongly coupled nuclear spin leads to a broadening of the coherence time peak compared to VVA, and to a decrease in the maximum of T_2 (0.930(14) ms for VVB vs. 1.17(4) ms for VVA). We note that the measured and computed zero-field Hahn-echo coherence times agree even without applying any charge depletion to the sample, suggesting that the electric noise has a minor impact on T_2 .

V. NATURE OF NUCLEAR NOISE IN SOLID-STATE QUBITS

Having validated the predictions of the gCCE with several experiments, we can now analyze the nature of the nuclear noise in the decoherence processes of the $kh\text{-}V_C V_{Si}$ and the axial divacancies.

We computed the coherence time of the $kh\text{-}V_C V_{Si}$ at zero field (0 T), where a clock

transition occurs, and at $B_z = 0.1$ T where we expect the basal and axial divacancies to exhibit similar coherence properties. We considered eigenstates of \hat{S}_z as qubit levels at 0.1 T. We found that at both zero and strong magnetic fields, the Ramsey decay is limited by static thermal noise arising from the entanglement of the qubit with pure states of the bath, which remain unchanged in time [31]:

$$\hat{\rho}(0) \otimes \sum_B p_B |B\rangle \langle B| \rightarrow \sum_B p_B \hat{\rho}_B(t) \otimes |B\rangle \langle B| \quad (8)$$

Indeed our calculations of T_2^* for the kh - $V_C V_{Si}$ in the weakly-coupled bath (Fig.6a, b) show that the inhomogeneous coherence time depends on the hyperfine parameters only through the average bath coupling ($\sqrt{\sum_i A_{iz}^2}$), as expected in the case of static thermal noise. [38].

The nature of noise is different in Hahn-echo experiments, where the π -pulse removes the static part of the noise dominating the Ramsey decay, and T_2 depends only on the dynamical fluctuations of the magnetic field due to nuclear spins flips [31]. If the flips are completely random, the decay rates originate primarily from the accumulation of random phases due to dynamical fluctuations; in this case the noise is by definition classical and the variance of the noise distribution is given by $\sum_i A_{iz}^2$ [39]. Therefore we expect the coherence time to vary linearly as a function of $\sqrt{\sum_i A_{iz}^2}$ in systems where the noise is classical[40]. On the other hand, when the back action of the central spin is dominant (i.e. the dynamics of the nuclear bath is strongly influenced by the electron spin state [31]), the coherence dynamics deviates from that predicted using classical approximations [41]. Fig.6c shows T_2 of kh - $V_C V_{Si}$ as a function of $\sqrt{\sum_i A_{iz}^2}$ in the zero and strong field regimes. At zero field, T_2 varies as $\sqrt{\sum_i A_{iz}^2}$, with more than an order of magnitude difference in $\sqrt{\sum_i A_{iz}^2}$ between the different configurations. This dependence suggests a stochastic nature of the noise at clock transitions and is consistent with the results reported for bismuth qubits in silicon [34]. At strong fields, T_2 is instead independent on the average coupling to the bath, consistent with the quantum nature of the noise, expected in this regime. These results show that the noise affecting Hahn-echo experiments is different at clock transitions and in the strong field regime, and the transition from classical to quantum noise may be tuned by simply varying the applied magnetic field.

We note that the differences in the nature of the noise is not sufficient to explain why the average value of T_2 at the clock transition of the basal divacancy is similar to the one at strong field (1.15 ms vs 1.4 ms). This similarity arises from the combination of two

competing effects: strong electron spin back-action, leading in principle to a reduction in coherence time, and the Zeeman splitting of nuclear spins, having instead the opposite effect. We can isolate the effect of the electron spin's strong back-action on coherence time, by considering a hypothetical kh - $V_C V_{Si}$ with $E = 0$ MHz at zero magnetic field (Fig.6c, 0 T, no E). We found that the T_2 of this system is independent from $\sqrt{\sum_i A_{iz}^2}$, and the ensemble average T_2 is 0.2 ms, significantly smaller than the one obtained for the clock transition, confirming that the electron back-action is indeed responsible for an increase in the decoherence rate. At strong magnetic field, the Zeeman splitting of the nuclear spins is instead responsible for a decrease in decoherence rates. The splitting can be larger than both the interaction strength between nuclear spins and the hyperfine coupling, leading to the suppression of spin non-conserving flips [42]. Only the secular pairwise flip-flops of nuclear spins with the same gyromagnetic ratio ($\uparrow\downarrow \leftrightarrow \downarrow\uparrow$) are possible in this regime [5, 43], thus greatly reducing the number of possible spin flips and decreasing the decoherence rate. (Fig.2b).

VI. ENGINEERING QUBIT PROTECTION AT A CLOCK TRANSITION

It is interesting to analyze in detail the effect of the magnitude of the transverse component of the ZFS on coherence protection. In order to do so, we investigated how coherence times vary as a function of a hypothetical change in E for the kh - $V_C V_{Si}$, within a weakly coupled nuclear bath (Fig.7(a)). We find that the ensemble averaged coherence time scales sublinearly as a function of the transverse ZFS ($T_2 \approx 0.34E^{0.43}$, $T_2^* \approx 0.03E^{0.61}$; see SI for the distribution of single defect coherence times). Our calculations show that defects with large transverse ZFS will exhibit substantially higher protection from magnetic noise.

In particular, we predict the coherence time of the hk - $V_C V_{Si}$ basal divacancy. hk - $V_C V_{Si}$ has significantly higher transverse ZFS than kh - $V_C V_{Si}$ ($E = 82.0$ MHz), and similar longitudinal ZFS ($D = 1.222$ GHz) [33]. The total distribution of the T_2 and T_2^* as a function of the magnetic field for different spatial configurations of the weakly coupled nuclear bath is shown in Fig.7(b, c) for both basal defects. We can see that there is a significant variability in the value of the coherence time at $B = 0$. The increase in the transverse ZFS leads both to a significant increase in the maximum value of the coherence time and to an increased robustness towards the external magnetic field. The ensemble average zero field $T_2^* = 380 \mu\text{s}$

of hk - $V_C V_{Si}$ is predicted to be 2.3 times higher than the one of kh - $V_C V_{Si}$, and the $T_2 = 2.12$ ms is found to be increased by a factor of 1.8, in a good agreement with Fig.7a. In the presence of a strong field (0.1 T) the ensemble average coherence time for both basal divacancies is the same: $T_2^* = 0.7 \mu s$, $T_2 = 1.4$ ms, which confirms that the large transverse ZFS is the main driving force for an increased coherence protection in the hk - $V_C V_{Si}$.

Our results for the different basal divacancies show that by engineering high zero field splitting either by selecting different defects, or applying the strain to the system [44], one can achieve substantial increase in the coherence time.

VII. CONCLUSIONS

Understanding the relation between the electronic structure of spin defects and their coherence properties is pivotal to optimizing the conditions for solid-state qubit applications. In this work, we proposed a general computational approach to predict the impact of the dynamics of a central spin on the qubit coherence properties, and we investigated the effect of the nuclear spin bath at avoided crossings for divacancies in SiC. We validated our results with measurements of Ramsey fringes and Hahn-echo coherence times and found excellent agreement between theory and experiments, thus providing a robust strategy to uncover the effect of the interaction of nuclear spins on solid-state qubits' decoherence over a wide range of applied magnetic fields.

Applying charge depletion [36] to electrically improve coherence, we were able to experimentally isolate and elucidate the duality of the nuclear bath impact on clock transitions' dynamics. We discovered that in the presence of strongly coupled nuclear spins, multiple clock transitions in the frequency spectrum of the spin qubit can emerge. We identified and characterized the nuclei with high hyperfine coupling in these systems; the initialization of these nuclear spins should allow one to achieve significantly higher coherence times under applied magnetic fields, while the nuclear-spin dependent spectral features provides guidance for the development of a new class of electron-nuclear two-qubit gates. We found that the effect of weakly coupled nuclear spins can be treated as a stochastic classical noise at the clock transition, and that the total amplitude of the coupling is a good descriptor of the coherence time. We further probed the classical-to-quantum transition of the noise and showed how a tunable back action of the electronic spin emerges with applied magnetic

fields.

In sum, the theoretical approach developed in this work allows for the predictions of the dynamical and decoherence properties of solid-state qubit systems with complex spin degrees of freedom, in the presence of clock transitions and over a wide range of magnetic fields. Here we focused on specific defects in SiC, but the approach is general and can be used to describe several other systems of interest such as molecular qubits with multiple clock transitions [45], bismuth donor spin qubits in silicon [13], and other solid-state centers with complex energy structure. Combined with *ab initio* predictions of the spin Hamiltonian parameters [46], our approach paves the way to optimizing and eventually designing the coherence properties of spin qubits yet to be explored experimentally.

VIII. ACKNOWLEDGEMENTS

This work made use of resources provided by the University of Chicago’s Research Computing Center, the UChicago MRSEC (NSF DMR-1420709) and Pritzker Nanofabrication Facility, which receives support from the SHyNE, a node of the NSF’s National Nanotechnology Coordinated Infrastructure (NSF ECCS-1542205). M.M.O. and G.G. were supported by AFOSR FA9550-19-1-0358, H.M. by the UChicago MRSEC (NSF DMR-1420709). K.C.M., J.P.B., C.P.A., A.B., and D.D.A. were supported by AFOSR FA9550-19-1-0358, DARPA D18AC00015KK1932, and ONR N00014-17-1-3026.

M.O. developed the model and conducted the dynamics calculations. H.M. performed the *ab initio* DFT calculations. M.O., K.C.M., and J.P.B. designed the experiments. K.C.M. and J.P.B. performed the experiments. M.O., K.C.M., and J.P.B. analyzed the data. C.P.A. fabricated the sample. K.C.M. and J.P.B. developed the confocal microscope setup, with the assistance of A.B. D.D.A. advised on all experimental efforts. G.G. advised on theoretical efforts and supervised the project. All authors contributed to the writing of the manuscript.

Appendix A: Experimental Measurements of the kh - $V_C V_{Si}$ coherence properties

Our 4H-SiC sample consists of a 20 μm high-purity i-type SiC layer epitaxially grown on a 4° off-axis miscut of the Si face of a high-purity semi-insulating SiC substrate (serial number A3177-14, Norstel AB). Neutral divacancies are uniformly produced throughout the

epitaxial i-type 4H-SiC by electron irradiation with 2-MeV electrons at a dose of 3×10^{12} e/cm² followed by annealing at 850 °C for 30 min in Ar. A coplanar capacitor structure with a 10 μm gap width and a wire with 10 μm width made of Ti/Au are then patterned on the sample surface using electron beam lithography. Samples are cooled to 5 K in a closed-cycle cryostat (Cryostation s100, Montana Instruments).

The confocal microscope consists of a 905 nm excitation laser (QFLD-905-200S, QPhotonics) for off-resonant spin initialization, as well as a narrow-line tunable laser (DL pro, TOPTICA Photonics) for resonant spin readout. We focus these excitation beams through a microscope objective (LCPLN100XIR, Olympus). We detect the filtered optical signal with $\sim 80\%$ quantum efficiency using a low-jitter, low-dark count superconducting nanowire single-photon detector (SNSPD; Opus One, Quantum Opus). Electrical pulses from the SNSPD are counted using a data acquisition module (PCI-6259, National Instruments).

We drive the spin transition $|0\rangle \leftrightarrow |+\rangle$ using signal generators (SG396, Stanford Research Systems) modulated by an arbitrary waveform generator (HDAWG8, Zurich Instruments). The output of the signal generator is routed to the on-chip wire, which produces ac magnetic fields. Vector control of the magnetic field is obtained using a three-axis electromagnet outside the cryostat.

Appendix B: Calculation of cluster contributions in the gCCE

In order to evaluate the density matrix $\rho_C(t)$ in equation (4) we compute the evolution of the initial density matrix of a given cluster as:

$$\hat{\rho}_C(t) = \hat{U}_C \hat{\rho}_C(0) \hat{U}_C^\dagger \quad (\text{B1})$$

Using time ordered propagator \hat{U}_C .

The Hamiltonian used to model Ramsey experiments does not depend on time $\hat{H}(\tau) = \hat{H}_C$, and the propagator is trivial:

$$\hat{U}_C(t) = e^{-i\hat{H}_C t} \quad (\text{B2})$$

The Hamiltonian \hat{H}_C is equal to the system Hamiltonian (1), which contains only the central spin and a given cluster of nuclear spins:

$$\hat{H}_C = \hat{H}_e + \sum_{i \in C} \mathbf{S} \mathbf{A} \mathbf{I}_i - \sum_{i \in C} \gamma_n B_z \hat{I}_{z,i} + \sum_{i \neq j \in C} \mathbf{I}_i \mathbf{P} \mathbf{I}_j \quad (\text{B3})$$

Under the dynamical decoupling to the qubit, by assuming ideal instantaneous control pulses, we can write the propagator as follows:

$$\hat{U}_C(t) = \mathcal{T} \left[e^{-i\hat{H}_C\tau} e^{-i\sigma_{\{x,y,z\}} \frac{\phi}{2}} e^{-i\hat{H}_C\tau} \right]^N \quad (\text{B4})$$

where $\sigma_{\{x,y,z\}}$ is one of the Pauli matrices (depending on the type of the pulse), spanned by two qubit levels, τ is the delay between pulses, ϕ is the angle of rotation (equal to π for CPMG, XY4 sequences [47]; it may be varied to represent more complicated schemes [48]) and N is number of pulses. For example, the propagator used to model Hahn-echo experiments with a π rotation about the x axis is defined as follows:

$$\hat{U}_C^{HE}(t) = e^{-i\hat{H}_C\tau} e^{-i\sigma_x \frac{\pi}{2}} e^{-i\hat{H}_C\tau} \quad (\text{B5})$$

The Pauli matrices for qubit levels $|0\rangle$ and $|1\rangle$ are defined as:

$$\sigma_x = (|0\rangle\langle 1| + |1\rangle\langle 0|) \quad (\text{B6})$$

$$\sigma_y = i(|1\rangle\langle 0| - |0\rangle\langle 1|) \quad (\text{B7})$$

$$\sigma_z = (|0\rangle\langle 0| - |1\rangle\langle 1|) \quad (\text{B8})$$

When using Monte-Carlo sampling of the bath states, we perform the CCE calculations for each pure bath state separately. In the pure bath state, each nucleus is initialized in the spin up or spin down state, and in the mixed state each nuclear spin has a classical probability of being in one of the two states. We define the density matrix elements of the central spin as follows:

$$\hat{\rho}_{ab}(t) = \sum_B p_J \hat{\rho}_{ab}^J(t) \quad (\text{B9})$$

where the elements of the density matrix $\hat{\rho}_{ab}$ are written as a summation over pure bath states J , with elements $\hat{\rho}_{ab}^J$ and probability p_J . In the case of a completely randomized bath (the density matrix of each nuclear spin is equal to $I/2$), the probability p_J is the same for

all pure bath states. At the typical temperatures of the experiment (≥ 4 K) the nuclear bath can be considered completely randomized.

The procedure used to evaluate the density matrix elements is the following. First, we generate a set of random pure bath states. For each bath state we perform CCE calculations to obtain the electron spin density matrix. Finally, we compute the density matrix elements for the mixed bath state from equation (B9), and verify the convergence of density matrix elements $\rho_{ab}(t)$ with respect to the number of generated bath states (see Supplementary Information).

We add the mean field effect of the bath spins outside a given cluster, by adding the \hat{H}_{mf} term into the cluster Hamiltonian (B3). The mean field term is defined as:

$$\hat{H}_{\text{mf}} = \sum_{i \notin C} \left[A_{zz} \langle I_{z,i} \rangle \hat{S}_z + \sum_{j \in C} P_{zz} \langle I_{z,i} \rangle \hat{I}_{z,j} \right] \quad (\text{B10})$$

where $\langle I_{z,i} \rangle = \pm 1/2$, is the projection of the nuclear spin in the z direction. The sign depends on the initial state of the nuclei i in the given random bath state.

Appendix C: Calculations of hyperfine coupling of nuclear spins

The inhomogeneous coherence time T_2^* is directly related to the hyperfine couplings. Under weak magnetic fields, the nuclear spin flips can be induced by both the hyperfine coupling and dipolar-dipolar interactions between nuclear spins [42]; hence accurate predictions of the hyperfine parameters are necessary to correctly compute the Hahn-echo coherence time as well.

We performed *ab initio* Density Functional Theory (DFT) calculations to predict hyperfine coupling constants for nuclear spins at distances up to 1 nm from the defect and we used the point dipole approximation for spins at larger distances. DFT calculations using the PBE functional were carried out with the GIPAW code [49] using single-particle wavefunctions obtained with the Quantum Espresso code [50]. Wavefunctions are represented on a plane-wave basis with a kinetic energy cutoff of 40 Ry. GIPAW pseudopotentials [51] are used to model electron-ion interactions. Divacancies are modeled with $9 \times 5 \times 2$ orthorhombic supercells containing 1438 atoms and the Brillouin zone is sampled with the Γ point only.

We define a weakly coupled bath as a bath in which the nuclear spins do not change the energy splitting of the defect. We impose a cutoff of the hyperfine couplings of $A_{zz} < 1$ MHz present in the weakly coupled bath, which is of typical order of magnitude compared to strongly coupled nuclear spins in NV center [52, 53]. The ensemble dynamics throughout the text is shown for the weakly coupled bath.

-
- [1] E. D. Herbschleb, H. Kato, Y. Maruyama, T. Danjo, T. Makino, S. Yamasaki, I. Ohki, K. Hayashi, H. Morishita, M. Fujiwara, and N. Mizuochi, Ultra-long coherence times amongst room-temperature solid-state spins, *Nature Communications* **10**, 3766 (2019).
 - [2] L. Robledo, L. Childress, H. Bernien, B. Hensen, P. F. A. Alkemade, and R. Hanson, High-fidelity projective read-out of a solid-state spin quantum register, *Nature* **477**, 574 (2011).
 - [3] J. R. Weber, W. F. Koehl, J. B. Varley, A. Janotti, B. B. Buckley, C. G. Van de Walle, and D. D. Awschalom, Quantum computing with defects, *Proceedings of the National Academy of Sciences* **107**, 8513 (2010), <https://www.pnas.org/content/107/19/8513.full.pdf>.
 - [4] C. L. Degen, F. Reinhard, and P. Cappellaro, Quantum sensing, *Rev. Mod. Phys.* **89**, 035002 (2017).
 - [5] H. Seo, A. L. Falk, P. V. Klimov, K. C. Miao, G. Galli, and D. D. Awschalom, Quantum decoherence dynamics of divacancy spins in silicon carbide, *Nature Communications* **7**, 12935 (2016).
 - [6] A. M. Tyryshkin, S. Tojo, J. J. L. Morton, H. Riemann, N. V. Abrosimov, P. Becker, H.-J. Pohl, T. Schenkel, M. L. W. Thewalt, K. M. Itoh, and S. A. Lyon, Electron spin coherence exceeding seconds in high-purity silicon, *Nature Materials* **11**, 143 (2012).
 - [7] R. E. George, J. P. Edwards, and A. Ardavan, Coherent spin control by electrical manipulation of the magnetic anisotropy, *Phys. Rev. Lett.* **110**, 027601 (2013).
 - [8] W. M. Witzel and S. Das Sarma, Quantum theory for electron spin decoherence induced by nuclear spin dynamics in semiconductor quantum computer architectures: Spectral diffusion of localized electron spins in the nuclear solid-state environment, *Phys. Rev. B* **74**, 035322 (2006).
 - [9] M. H. Abobeih, J. Cramer, M. A. Bakker, N. Kalb, M. Markham, D. J. Twitchen, and T. H. Taminiau, One-second coherence for a single electron spin coupled to a multi-qubit nuclear-

- spin environment, *Nature Communications* **9**, 2552 (2018).
- [10] T. van der Sar, Z. H. Wang, M. S. Blok, H. Bernien, T. H. Taminiau, D. M. Toyli, D. A. Lidar, D. D. Awschalom, R. Hanson, and V. V. Dobrovitski, Decoherence-protected quantum gates for a hybrid solid-state spin register, *Nature* **484**, 82 (2012).
- [11] A. Reiserer, N. Kalb, M. S. Blok, K. J. M. van Bemmelen, T. H. Taminiau, R. Hanson, D. J. Twitchen, and M. Markham, Robust quantum-network memory using decoherence-protected subspaces of nuclear spins, *Phys. Rev. X* **6**, 021040 (2016).
- [12] A. Bourassa, C. P. Anderson, K. C. Miao, M. Onizhuk, H. Ma, A. L. Crook, H. Abe, J. Ul-Hassan, T. Ohshima, N. T. Son, G. Galli, and D. D. Awschalom, Entanglement and control of single nuclear spins in isotopically engineered silicon carbide, *Nature Materials* 10.1038/s41563-020-00802-6 (2020).
- [13] G. Wolfowicz, A. M. Tyryshkin, R. E. George, H. Riemann, N. V. Abrosimov, P. Becker, H.-J. Pohl, M. L. W. Thewalt, S. A. Lyon, and J. J. L. Morton, Atomic clock transitions in silicon-based spin qubits, *Nature Nanotechnology* **8**, 561 (2013).
- [14] M. H. Mohammady, G. W. Morley, and T. S. Monteiro, Bismuth qubits in silicon: The role of epr cancellation resonances, *Phys. Rev. Lett.* **105**, 067602 (2010).
- [15] K. C. Miao, J. P. Blanton, C. P. Anderson, A. Bourassa, A. L. Crook, G. Wolfowicz, H. Abe, T. Ohshima, and D. D. Awschalom, Universal coherence protection in a solid-state spin qubit, *Science* 10.1126/science.abc5186 (2020), <https://science.sciencemag.org/content/early/2020/08/12/science.abc5186.full.pdf>.
- [16] V. Ivády, Longitudinal spin relaxation model applied to point-defect qubit systems, *Phys. Rev. B* **101**, 155203 (2020).
- [17] A. Jarmola, V. M. Acosta, K. Jensen, S. Chemerisov, and D. Budker, Temperature- and magnetic-field-dependent longitudinal spin relaxation in nitrogen-vacancy ensembles in diamond, *Phys. Rev. Lett.* **108**, 197601 (2012).
- [18] Z.-S. Yang, Y.-X. Wang, M.-J. Tao, W. Yang, M. Zhang, Q. Ai, and F.-G. Deng, Longitudinal relaxation of a nitrogen-vacancy center in a spin bath by generalized cluster-correlation expansion method, *Annals of Physics* **413**, 168063 (2020).
- [19] W. F. Koehl, B. B. Buckley, F. J. Heremans, G. Calusine, and D. D. Awschalom, Room temperature coherent control of defect spin qubits in silicon carbide, *Nature* **479**, 84 (2011).
- [20] P. V. Klimov, A. L. Falk, D. J. Christle, V. V. Dobrovitski, and D. D.

- Awschalom, Quantum entanglement at ambient conditions in a macroscopic solid-state spin ensemble, *Science Advances* **1**, 10.1126/sciadv.1501015 (2015), <https://advances.sciencemag.org/content/1/10/e1501015.full.pdf>.
- [21] N. T. Son, C. P. Anderson, A. Bourassa, K. C. Miao, C. Babin, M. Widmann, M. Niethammer, J. Ul Hassan, N. Morioka, I. G. Ivanov, F. Kaiser, J. Wrachtrup, and D. D. Awschalom, Developing silicon carbide for quantum spintronics, *Applied Physics Letters* **116**, 190501 (2020), <https://doi.org/10.1063/5.0004454>.
- [22] D. J. Christle, A. L. Falk, P. Andrich, P. V. Klimov, J. U. Hassan, N. T. Son, E. Janzén, T. Ohshima, and D. D. Awschalom, Isolated electron spins in silicon carbide with millisecond coherence times, *Nature Materials* **14**, 160 (2015).
- [23] A. L. Crook, C. P. Anderson, K. C. Miao, A. Bourassa, H. Lee, S. L. Bayliss, D. O. Bracher, X. Zhang, H. Abe, T. Ohshima, E. L. Hu, and D. D. Awschalom, Purcell enhancement of a single silicon carbide color center with coherent spin control, *Nano Letters* **20**, 3427 (2020).
- [24] S. J. Whiteley, G. Wolfowicz, C. P. Anderson, A. Bourassa, H. Ma, M. Ye, G. Koolstra, K. J. Satzinger, M. V. Holt, F. J. Heremans, A. N. Cleland, D. I. Schuster, G. Galli, and D. D. Awschalom, Spin–phonon interactions in silicon carbide addressed by gaussian acoustics, *Nature Physics* **15**, 490 (2019).
- [25] K. C. Miao, A. Bourassa, C. P. Anderson, S. J. Whiteley, A. L. Crook, S. L. Bayliss, G. Wolfowicz, G. Thiering, P. Udvarhelyi, V. Ivády, H. Abe, T. Ohshima, Á. Gali, and D. D. Awschalom, Electrically driven optical interferometry with spins in silicon carbide, *Science Advances* **5**, 10.1126/sciadv.aay0527 (2019), <https://advances.sciencemag.org/content/5/11/eaay0527.full.pdf>.
- [26] W. Yang and R.-B. Liu, Quantum many-body theory of qubit decoherence in a finite-size spin bath, *Phys. Rev. B* **78**, 085315 (2008).
- [27] M. Ye, H. Seo, and G. Galli, Spin coherence in two-dimensional materials, *npj Computational Materials* **5**, 44 (2019).
- [28] W.-L. Ma, G. Wolfowicz, N. Zhao, S.-S. Li, J. J. Morton, and R.-B. Liu, Uncovering many-body correlations in nanoscale nuclear spin baths by central spin decoherence, *Nature Communications* **5**, 4822 (2014).
- [29] S. J. Balian, G. Wolfowicz, J. J. L. Morton, and T. S. Monteiro, Quantum-bath-driven decoherence of mixed spin systems, *Phys. Rev. B* **89**, 045403 (2014).

- [30] G.-L. Zhang, W.-L. Ma, and R.-B. Liu, Cluster-correlation expansion for studying decoherence of clock transitions in spin baths (2020), arXiv:2007.00412.
- [31] W. Yang, W.-L. Ma, and R.-B. Liu, Quantum many-body theory for electron spin decoherence in nanoscale nuclear spin baths, *Reports on Progress in Physics* **80**, 016001 (2016).
- [32] W. M. Witzel, M. S. Carroll, L. Cywiński, and S. Das Sarma, Quantum decoherence of the central spin in a sparse system of dipolar coupled spins, *Phys. Rev. B* **86**, 035452 (2012).
- [33] A. L. Falk, B. B. Buckley, G. Calusine, W. F. Koehl, V. V. Dobrovitski, A. Politi, C. A. Zorman, P. X.-L. Feng, and D. D. Awschalom, Polytype control of spin qubits in silicon carbide, *Nature Communications* **4**, 1819 (2013).
- [34] W.-L. Ma, G. Wolfowicz, S.-S. Li, J. J. L. Morton, and R.-B. Liu, Classical nature of nuclear spin noise near clock transitions of bi donors in silicon, *Phys. Rev. B* **92**, 161403(R) (2015).
- [35] P. Jamonneau, M. Lesik, J. P. Tetienne, I. Alvizu, L. Mayer, A. Dréau, S. Kosen, J.-F. Roch, S. Pezzagna, J. Meijer, T. Teraji, Y. Kubo, P. Bertet, J. R. Maze, and V. Jacques, Competition between electric field and magnetic field noise in the decoherence of a single spin in diamond, *Phys. Rev. B* **93**, 024305 (2016).
- [36] C. P. Anderson, A. Bourassa, K. C. Miao, G. Wolfowicz, P. J. Mintun, A. L. Crook, H. Abe, J. Ul Hassan, N. T. Son, T. Ohshima, and D. D. Awschalom, Electrical and optical control of single spins integrated in scalable semiconductor devices, *Science* **366**, 1225 (2019), <https://science.sciencemag.org/content/366/6470/1225.full.pdf>.
- [37] G. Wolfowicz, C. P. Anderson, A. L. Yeats, S. J. Whiteley, J. Niklas, O. G. Poluektov, F. J. Heremans, and D. D. Awschalom, Optical charge state control of spin defects in 4h-sic, *Nature Communications* **8**, 1876 (2017).
- [38] I. A. Merkulov, A. L. Efros, and M. Rosen, Electron spin relaxation by nuclei in semiconductor quantum dots, *Phys. Rev. B* **65**, 205309 (2002).
- [39] B. Gu and I. Franco, When can quantum decoherence be mimicked by classical noise?, *The Journal of Chemical Physics* **151**, 014109 (2019), <https://doi.org/10.1063/1.5099499>.
- [40] D. Stanek, C. Raas, and G. S. Uhrig, From quantum-mechanical to classical dynamics in the central-spin model, *Phys. Rev. B* **90**, 064301 (2014).
- [41] P. Huang, X. Kong, N. Zhao, F. Shi, P. Wang, X. Rong, R.-B. Liu, and J. Du, Observation of an anomalous decoherence effect in a quantum bath at room temperature, *Nature Communications* **2**, 570 (2011).

- [42] N. Zhao, S.-W. Ho, and R.-B. Liu, Decoherence and dynamical decoupling control of nitrogen vacancy center electron spins in nuclear spin baths, *Phys. Rev. B* **85**, 115303 (2012).
- [43] L.-P. Yang, C. Burk, M. Widmann, S.-Y. Lee, J. Wrachtrup, and N. Zhao, Electron spin decoherence in silicon carbide nuclear spin bath, *Phys. Rev. B* **90**, 241203(R) (2014).
- [44] A. L. Falk, P. V. Klimov, B. B. Buckley, V. Ivády, I. A. Abrikosov, G. Calusine, W. F. Koehl, A. Gali, and D. D. Awschalom, Electrically and mechanically tunable electron spins in silicon carbide color centers, *Phys. Rev. Lett.* **112**, 187601 (2014).
- [45] M. Shiddiq, D. Komijani, Y. Duan, A. Gaita-Ariño, E. Coronado, and S. Hill, Enhancing coherence in molecular spin qubits via atomic clock transitions, *Nature* **531**, 348 (2016).
- [46] K. Ghosh, H. Ma, V. Gavini, and G. Galli, All-electron density functional calculations for electron and nuclear spin interactions in molecules and solids, *Phys. Rev. Materials* **3**, 043801 (2019).
- [47] G. de Lange, Z. H. Wang, D. Ristè, V. V. Dobrovitski, and R. Hanson, Universal dynamical decoupling of a single solid-state spin from a spin bath, *Science* **330**, 60 (2010).
- [48] S. S. Hegde, J. Zhang, and D. Suter, Efficient quantum gates for individual nuclear spin qubits by indirect control, *Phys. Rev. Lett.* **124**, 220501 (2020).
- [49] <https://github.com/dceresoli/qe-gipaw>, accessed: Jul. 14, 2020.
- [50] P. Giannozzi, S. Baroni, N. Bonini, M. Calandra, R. Car, C. Cavazzoni, D. Ceresoli, G. L. Chiarotti, M. Cococcioni, I. Dabo, A. D. Corso, S. de Gironcoli, S. Fabris, G. Fratesi, R. Gebauer, U. Gerstmann, C. Gougoussis, A. Kokalj, M. Lazzeri, L. Martin-Samos, N. Marzari, F. Mauri, R. Mazzarello, S. Paolini, A. Pasquarello, L. Paulatto, C. Sbraccia, S. Scandolo, G. Sclauzero, A. P. Seitsonen, A. Smogunov, P. Umari, and R. M. Wentzcovitch, Quantum espresso: a modular and open-source software project for quantum simulations of materials, *J. Phys.: Condens. Matter* **21**, 395502 (2009).
- [51] <https://sites.google.com/site/dceresoli/pseudopotentials>, accessed: Jul. 14, 2020.
- [52] J. Yun, K. Kim, and D. Kim, Strong polarization of individual nuclear spins weakly coupled to nitrogen-vacancy color centers in diamond, *New Journal of Physics* **21**, 093065 (2019).
- [53] A. Dréau, J.-R. Maze, M. Lesik, J.-F. Roch, and V. Jacques, High-resolution spectroscopy of single nv defects coupled with nearby ^{13}C nuclear spins in diamond, *Phys. Rev. B* **85**, 134107 (2012).

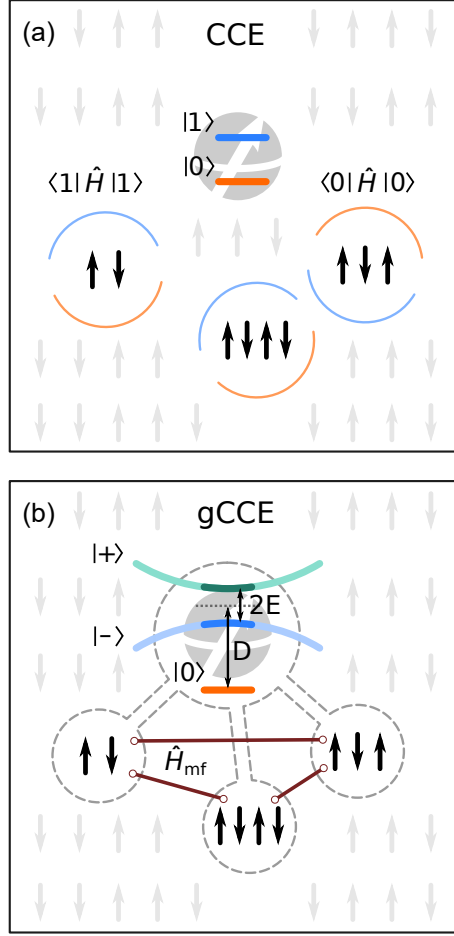


FIG. 1. Schematic representation of the conventional (CCE) and generalized (gCCE) Cluster-Correlation Expansion methods. (a) In the conventional CCE the evolution of each bath cluster is conditioned on two qubit levels, $|0\rangle$ and $|1\rangle$, computed using the projected Hamiltonian $\hat{H}^{(0/1)} = \langle 0/1| \hat{H} |0/1\rangle$. (b) In the gCCE method each cluster includes the central spin levels (denoted as $|+\rangle$, $|-\rangle$, and $|0\rangle$) for spin-1 with nonzero longitudinal D and transverse E zero field splitting (ZFS). The interactions between clusters are treated at the mean field level (\hat{H}_{mf}), using Monte-Carlo sampling of bath states.

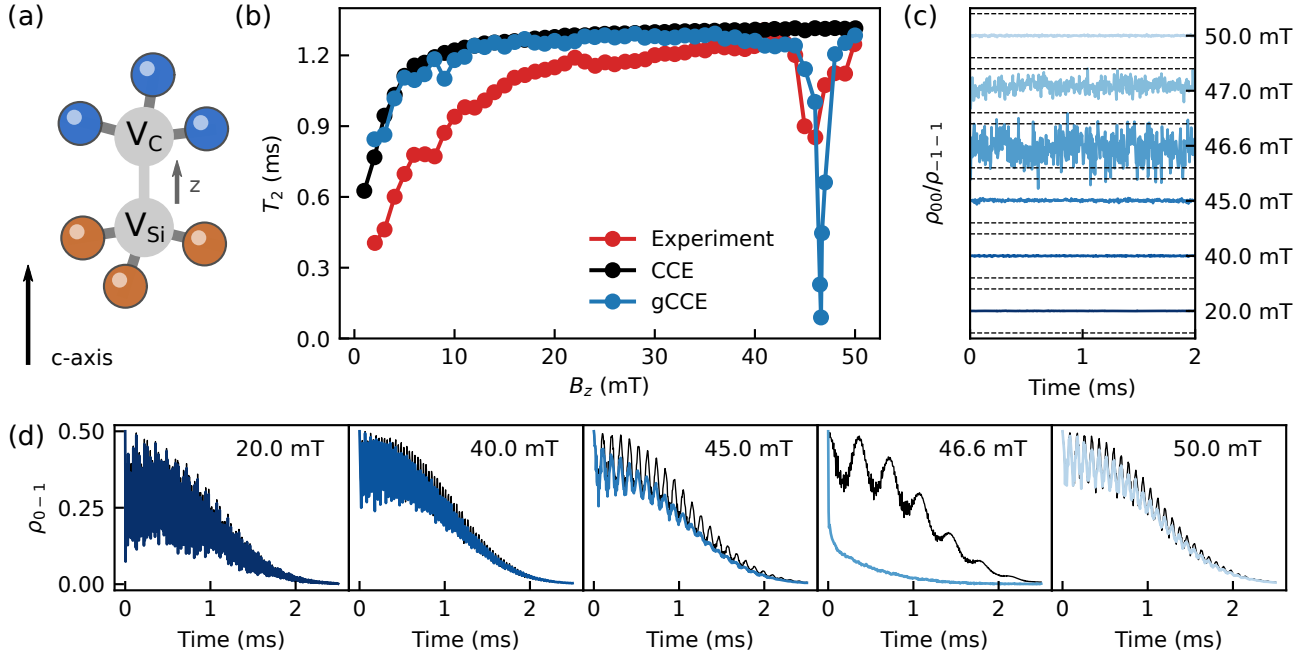


FIG. 2. Ensemble Hahn-echo coherence of the axial kk -divacancy in 4H-SiC. (a) Schematic representation of the axial kk -divacancy. (b) Coherence time T_2 (blue dots) as a function of the magnetic field B_z . The experimental results (red dots) and conventional CCE predictions (black dots) are from [5]. (c) The oscillations in the ratio of the diagonal elements of the density matrix of the divacancy as a function of time for various values of the magnetic field. The dashed lines show the $\pm 2\%$ range. (d) The off-diagonal elements of the density matrix for different magnetic fields computed using the gCCE method with Monte-Carlo sampling of the bath states (color) and using the conventional CCE (black).

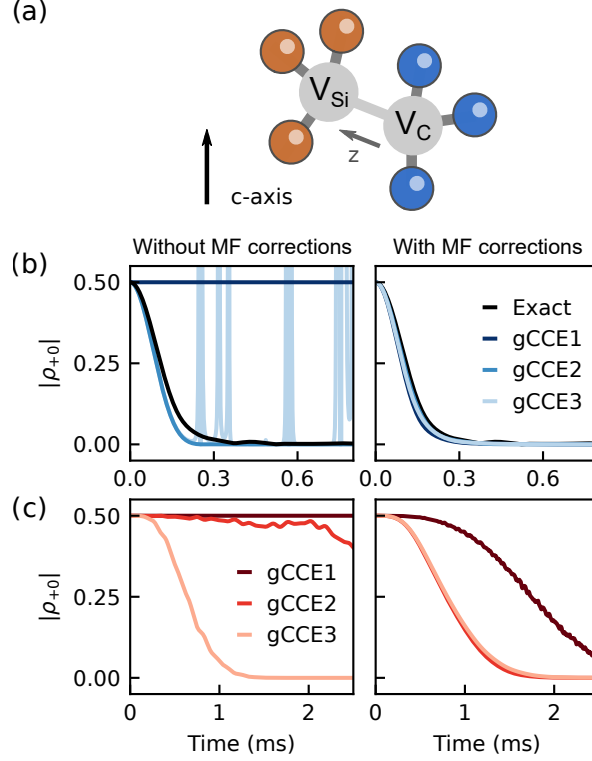


FIG. 3. Single defect coherence of the basal kh -divacancy in 4H-SiC predicted by different theoretical approximations. (a) Schematic representation of the basal kh -divacancy. (b, c) The absolute value of the off-diagonal elements of the density matrix $|\rho_{0+}| = |\langle 0 | \hat{\rho} | + \rangle|$ for one random nuclear configuration corresponding to Ramsey (b) and Hahn-echo (c) experiments. The results of the gCCE at different orders (from 1 to 3) without mean field (MF) interactions are shown on the left hand side, with mean field corrections are on the right hand side. The exact solution for a bath of 9 nuclear spins for the Ramsey decay is shown as a black line.

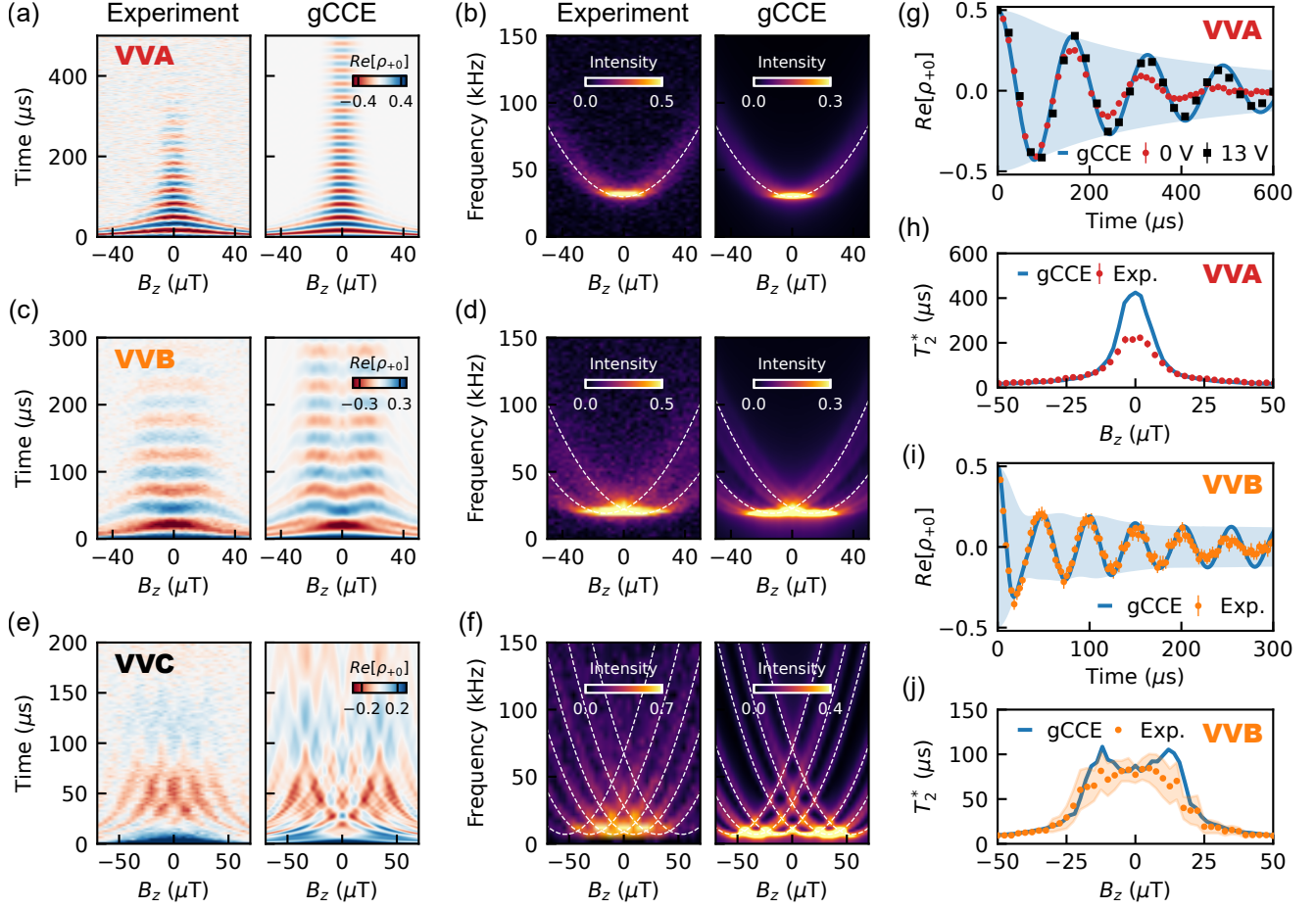


FIG. 4. Ramsey interferometry for three experimental kh - $V_C V_{\text{Si}}$ systems. (a-f) Ramsey precession and frequency spectrum for a defect with only weakly coupled nuclear spins (VVA, a, b), with one (VVB, c, d), and with three strongly coupled nuclear spins (VVC, e, f). For each defect we show theoretical predictions and experimental results. White dashed lines show the positions of the hyperbolae (see Eq. 6). (g) Measured Ramsey precession of VVA at zero field with (black) or without (red) charge depletion (see text), compared to the theoretical prediction (blue). The shaded area corresponds to the theoretically predicted decay. (h, j) Distribution of T_2^* for VVA (h) and VVB (j) as a function of the magnetic field (B_z). Shaded area in (j) shows the error of the fit. (i) Measured Ramsey precession of VVB at weak applied magnetic field compared to the theoretical prediction. Error bars correspond to 2SD.

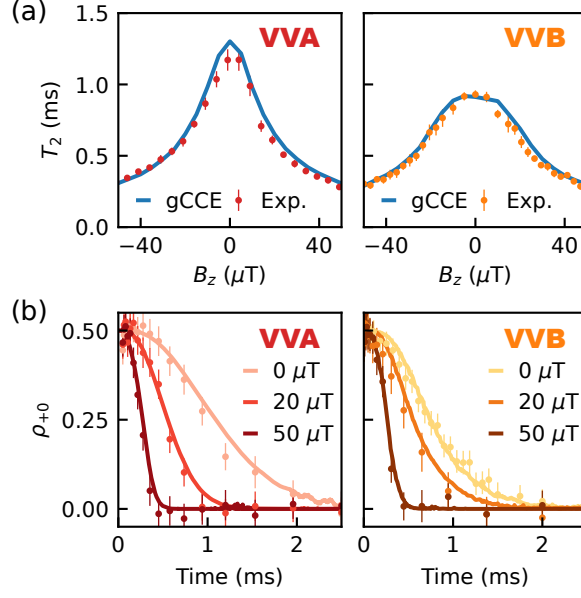


FIG. 5. Single defect Hahn-echo coherence time of $kh\text{-}V_C V_{Si}$. (a) Distribution of T_2 for VVA (left) and VVB (right) as a function of the magnetic field B_z (VVA and VVB are the same defects represented in Fig.4). (b) The Hahn echo decay for three different values of the magnetic field. Solid lines correspond to theoretical predictions, points to experimental measurements. Error bars correspond to 2SD.

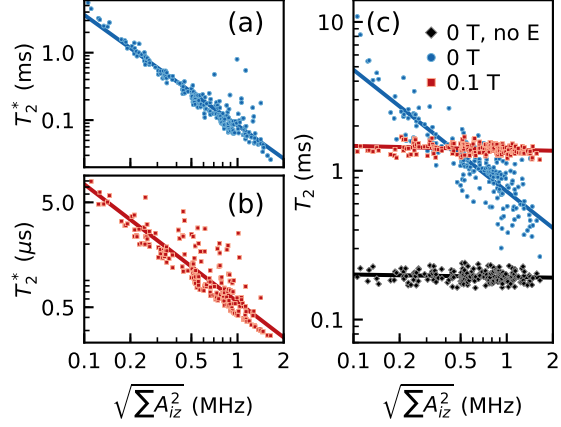


FIG. 6. Single defect coherence times T_2^* and T_2 of the kh - $V_C V_{S_i}$ at zero and high magnetic field for different bath coupling. (a, b) T_2^* for zero (a) and high (b) field as a function of the square root of the sum of squares of the hyperfine couplings with the bath spins $\sqrt{\sum_i A_{iz}^2}$. Significant deviations from the least squares fit (solid lines) are present for systems containing single nuclear spins with high hyperfine coupling, and the coherence decay may not be approximated by a single exponential [42]. (c) T_2 for zero (blue) and high (red) magnetic fields, and for an hypothetical system with $E = 0$ MHz at zero field (black). All calculations are performed for SiC with natural isotope concentration for the weakly coupled nuclear bath.

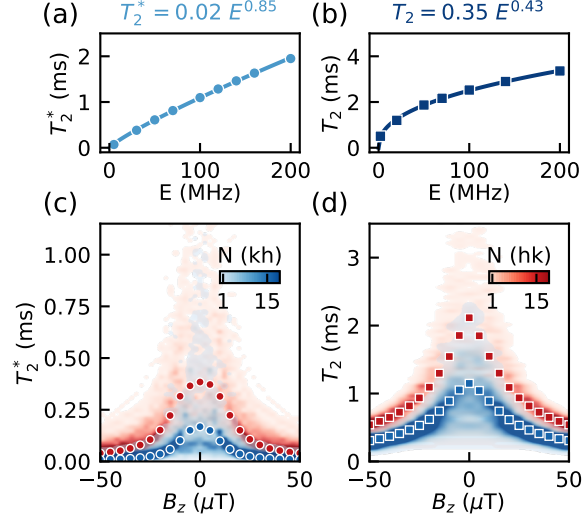


FIG. 7. Dependence of the coherence time on the transverse zero-field-splitting (ZFS). (a, b) Coherence times T_2^* (a) and T_2 (b) of kh - $V_C V_{Si}$ with different hypothetical values of transverse ZFS E . (c, d) The heat map of the single defect T_2^* (T_2) for 120 different nuclear spin configurations of both hk - $V_C V_{Si}$ (red) and kh - $V_C V_{Si}$ (blue) as a function of magnetic field. The color corresponds to the number of configurations with a given T_2^* (T_2) at the given magnetic field. The circles (squares) indicate the ensemble averaged coherence time.